Performance Comparison of 2D Nickel Phosphate Nanoparticles Prepared Via Sonochemical and Microwave-Assisted Hydrothermal Routes for Supercapattery

Norshahirah Mohamad Saidi[1], Artiqah Khairudin[2], Lijie Li[3], Muhammad Amirul Aizat Mohd Abdah[1], Ong Gerard[1,4], Yee Seng Tan[5], M Khalid[1,6,7], F. Khan[8], Muhammad Norhaffis Mustafa[1], Arshid Numan1*

[1]Sunway Centre for Electrochemical Energy and Sustainable Technology (SCEEST), School of Engineering and Technology, Sunway University, No. 5, Jalan Universiti, Bandar Sunway, Subang Jaya, Selangor 47500, Malaysia
[2]Department of Applied Physics, Faculty of Science and Technology, Universiti Kebangsaan Malaysia (UKM), Bangi 43600, Selangor, Malaysia
[3]Multidisciplinary Nanotechnology Centre, College of Engineering, Swansea University, Swansea SA1 8EN, United Kingdom
[4]Centre for Ionics University of Malaya, Department of Physics, Faculty of Science, University of Malaya, 50603 Kuala Lumpur, Malaysia
[5]Research Centre for Crystalline Materials, School of Medical and Life Sciences, Sunway University, No. 5, Jalan Universiti, Bandar Sunway, Subang Jaya, Selangor 47500, Malaysia
[6]Uttaranchal University, Dehradun, 248007 Uttarakhand, India
[7]Division of Research and Development, Lovely Professional University, Phagwara, 144411, Punjab, India
[8]Department of Physics, The University of Haripur, 22620 KP-Pakistan

*Corresponding author: numan.arshed@yahoo.com

Abstract:

Metal phosphates are broadly applied in electrochemical energy storage applications because of their abundance in nature, cost-effectiveness, and excellent electrochemical performance. Herein, we compare the performance of nickel phosphate ($Ni_3(PO_4)_2$) prepared through sonochemical and microwave-assisted hydrothermal reaction (MW) synthesis routes for supercapattery. These methods are efficient, rapid, and facile, yielding a high quantity of nanoparticles. Field Emission Scanning Electron Microscopy reveals that $Ni_3(PO_4)_2$ nanoparticles synthesized via the MW method are smaller than those produced via the sonochemical method. X-ray diffraction analysis confirmed that the MW method, followed by calcination at 200℃ for 3 hours ($NiPO_4$-MWB sample), produces amorphous nanoparticles, providing more exposure to redox-active sites. This work demonstrates that the $NiPO_4$-

MWB sample exhibits the highest specific capacity of 256.54 C g^{-1} at a current density of 1 A g^{-1} compared to its counterpart electrode prepared via the sonochemical. A device fabricated using $NiPO_4$-MWB//activated carbon (AC) delivered an energy density of 10.33 Wh kg^{-1} at a power density of 750 W kg^{-1}, retaining 99.42% of its capacity after 5000 cycles. The notable capacity retention makes it an attractive candidate for supercapattery electrodes. These findings suggest that MW synthesis can be used for the rapid production of tailored nanoparticles for electrochemical energy storage applications.

Keywords: Nickel phosphate; sonochemical; microwave hydrothermal; supercapattery

1. Introduction

A continuous energy source is required to support the rapid advancement of technology in the industrial sector. Non-renewable energy sources, specifically fossil fuels, have been the predominant energy source for several decades. However, their usage has resulted in the emission of excessive amounts of greenhouse gases, thereby contributing to global warming. As a result, researchers have started shifting towards renewable energy sources like solar, wind, and hydropower as the primary sources of electricity. Nevertheless, the efficacy of these sources is constrained by the absence of an effective energy storage system with low internal resistance, which is crucial for energy buffering and storage[1]. Lithium-Ion Batteries (LIBs) have gained primary importance because they can store more charges and have a high specific energy of 75 – 200 Wh kg^{-1}. LIBs have several shortcomings despite widespread use, including prolonged charging periods, limited long-term stability, and susceptibility to catastrophic failure upon overcharging [2,3]. These limitations have prompted researchers to explore alternative battery chemistries that can mitigate these drawbacks while maintaining the impressive performance of LIBs.

Another promising energy storage system that has emerged is supercapacitors, classified into pseudocapacitors and electric double-layer capacitors (EDLCs) [4–6]. They have long-term stability

due to their high specific power density of 1-10 kW kg^{-1}. However, they also have flaws where they cannot store more energy due to low specific energy density of 0.1-10 Wh kg^{-1}. Based on the literature, it is evident that LIBs and supercapacitors exhibit unique strengths and weaknesses. While the former experiences a deficiency in specific power density, the latter confronts challenges with low specific energy density. To address these limitations, researchers have proposed a novel approach by synergistically leveraging the properties of electrode materials in a single device. This new device coined the "supercapattery," represents a promising advancement in energy storage technology [7]. Supercapattery, also known as an asymmetric electrochemical capacitor, combines the advantages of capacitors and batteries, making it a promising energy storage device.

Supercapattery offers higher energy storage capabilities than traditional supercapacitors but is lower than batteries [8,9]. It bridges the gap between supercapacitors' high power density and batteries' high energy density. This speciality allows them to store more energy per unit of volume or weight, providing a good balance between power and energy storage.

Supercapatteries can retain stored energy for longer periods than traditional capacitors, where capacitors discharge quickly when not in use due to their inherent leakage [8]. Moreover, supercapatteries offer a higher power density than batteries, meaning they can deliver and absorb energy quickly [10]. They can provide bursts of power, making them useful in applications that demand high-power bursts. Compared to batteries, supercapatteries generally have a much longer cycle life [10]. They can withstand many charge and discharge cycles without significant degradation, making them more durable and cost-effective in the long run. Supercapatteries are more environmentally friendly than certain types of batteries, such as those containing heavy metals or toxic chemicals [11,12]. They are often made using more sustainable materials and can be recycled more easily. It's worth noting that the specific advantages of supercapatteries can vary depending on the materials of the electrodes used.

Supercapattery can be assembled by combining a battery-type electrode as a positive and a capacitive-type electrode as a negative electrode. Carbonaceous materials are often chosen as capacitive-type

electrodes due to their large surface area and high conductivity [13]. Meanwhile, metal oxides [14–16], metal hydroxides [17–19], metal sulfides [20,21] and metal phosphates [22–24] are widely used as battery-type electrode materials. Amongst all, metal phosphate has garnered attention in energy storage applications due to its two-dimensional framework built from the strong coordinate bond between transition metals and phosphate [25]. This structure can impressively contribute to the active material's high specific capacity and excellent structural stability. Furthermore, it has good mechanical properties as it can resist deformation and stabilize ions in transition metals [23]. The performance of a supercapattery mainly depends on the properties of active materials. These properties also can be controlled through a synthesis method [26]. Co-precipitation [27,28], sonochemical [29–32], conventional hydrothermal [33,34], and microwave-assisted hydrothermal [35] are common methods for synthesizing metal phosphates. Different synthesis methods could produce different structural, morphologies and shapes, affecting the device's electrochemical performance. Nonetheless, it is essential to acknowledge the best synthesis techniques as they control the electrodes' morphology, particle size and crystallinity.

The most straightforward technique is co-precipitation, involving only a solution and stirring on a hotplate magnetic stirrer. However, this method yields larger particles (in the micrometre range), which detrimentally impacts device performance. This size limitation reduces the availability of electrochemically active sites for facilitating redox reactions at the electrodeelectrolyte interface [36]. These redox-active sites play a critical role, acting as catalysts to enhance electrode reaction kinetics [37] and offering alternate pathways for charge transfer at the electrode-electrolyte interface. Thus, achieving a smaller particle size becomes a crucial criterion for better active material as it can increase redox-active sites within the electrode, subsequently enhancing overall performance. One approach to producing smaller particle sizes is through sonochemical synthesis. Ultrasonic waves applied during the sonochemical process would produce a finer particle (i.e., nano-sized) [38]. Omar et al. synthesized small-size nickel phosphate nanoparticles of 70 nm using the sonochemical method [39]. Their work's highest energy and power densities are 76 Wh kg^{-1} and 559 W kg^{-1}, respectively. Another

synthesis method that can produce smaller particle sizes is conventional hydrothermal and microwaveassisted hydrothermal. These methods used high sealed pressure and high temperature during the process. The only thing that matters to them is that conventional hydrothermal uses outer stainless steel, and the inner Teflon tube leads to slow conduction of heat and takes a long time for this process. On the other hand, microwave-assisted hydrothermal is less time-consuming as it uses outer ceramic and inner Teflon tube, which helps rapid heating and shortens reaction time. Ong et al. reported on the binder-free nickel-copper phosphate [7] and nickel-manganese phosphate [40] using a microwave-assisted hydrothermal technique. Their work showed outstanding performance with the maximum specific capacity of 1500 C g^{-1} achieved at 3 A g^{1} for the nickel-manganese phosphate electrode materials.

Herein, we synthesized nickel phosphate ($Ni_3(PO_4)_2$) nanoparticles by using two different synthesis routes (i) sonochemical method ($NiPO_4$-SA) and (ii) microwave-assisted hydrothermal method ($NiPO_4$-MWA). Samples prepared by both synthesis techniques were also calcined at 200 °C for three hours. The performance of all the electrode materials was tested through a string of cyclic voltammetry cycle (CV), galvanometric charge-discharge (GCD) and electrochemical impedance spectroscopy (EIS) studies. Besides, the best electrode material was tested in a two-electrode cell configuration to investigate its real-time performance. Our results imply that a microwave-assisted hydrothermal method can broadly impact the properties of nickel phosphate particles, including their morphology and structural and electrical properties.

2. Experimental

2.1 Materials

Nickel (II) chloride hexahydrate ($NiCl_2.6H_2O$), Di-sodium hydrogen orthophosphate anhydrous (Na_2HPO_4), N-Methyl-2-pyrrolidone (NMP), acetone (C_3H_6O), ethanol (C_2H_6O), and hydrochloric acid (HCl ~ 37 %) were used as received from Fisher Scientific, Malaysia.

Polyvinylidene fluoride (PVDF) and carbon black were used as received from Alfa Aesar. Activated carbon (AC) was obtained from Acros Organic, and potassium hydroxide (KOH) pallets were purchased from Merck. All these materials were used without further purification. Deionized water was used throughout the experiments. Nickel foam (Goodfellow, UK) was cut into 2 x 1 cm sheets and used as a substrate throughout the experiment. The substrates were prewashed using an ultrasonicate bath for 10 minutes in the presence of 0.5 M hydrochloric acid, deionized (DI) water and ethanol subsequently. The washed substrates were dried in a vacuum oven at 60 °C for 12 hours.

2.2 Synthesis of $Ni_3(PO_4)_2$ nanoparticle via the sonochemical method

The synthesis of $Ni_3(PO_4)_2$ nanoparticles started by preparing two precursor solutions. A metal precursor solution was prepared by dissolving 0.1 M nickel (II) chloride hexahydrate ($NiCl_2.6H_2O$) in 40 mL of DI water. Then, the second solution containing 0.2 M anhydrous sodium hydrogen phosphate (Na_2HPO_4) was prepared separately in 40 mL of DI water and added dropwise (at 2 mL/min rate) in $NiCl_2.6H_2O$ solution under constant stirring. The mixture was kept under continuous stirring for another 30 minutes before being subjected to ultrasonication using a horn sonicator for 40 min at a pulse amplitude of 60 watts, pulse on-time 2 s, and off time 1 s. A light green precipitate was formed, washed with deionized water and ethanol, and dried in a hot air oven at 90 °C for 12 hours. The dried sample was grounded using an agate mortar pestle and designated $NiPO_4$-SA. For comparison, $NiPO_4$-SB was prepared with a similar synthesis process followed by calcination in a muffle furnace at 200 °C for three hours.

2.3 Synthesis of $Ni_3(PO_4)_2$ nanoparticle via the microwave-assisted hydrothermal method

0.2 M Na_2HPO_4 solution was dropwise added into the 0.1 M $NiCl_2.6H_2O$ solution at a 2 mL/min rate under constant stirring. The mixture was stirred for another 30 minutes and then transferred into a Teflon tube. It was then placed in a microwave reactor (flexiWAVE, Milestone Inc.) for microwave-assisted hydrothermal reaction at 200 °C for 10 minutes under the heating rate of 5 °C per minute.

The precipitates are collected, washed, and dried in a hot air oven at 90 °C for 12 hours. The dried sample was designated as $NiPO_4$-MWA. Similarly, the same procedure was repeated, followed by calcination at 200 °C for 3 hours in a muffle furnace. The sample is labelled as $NiPO_4$-MWB. The synthesis processes for both methods are illustrated in Figure 1.

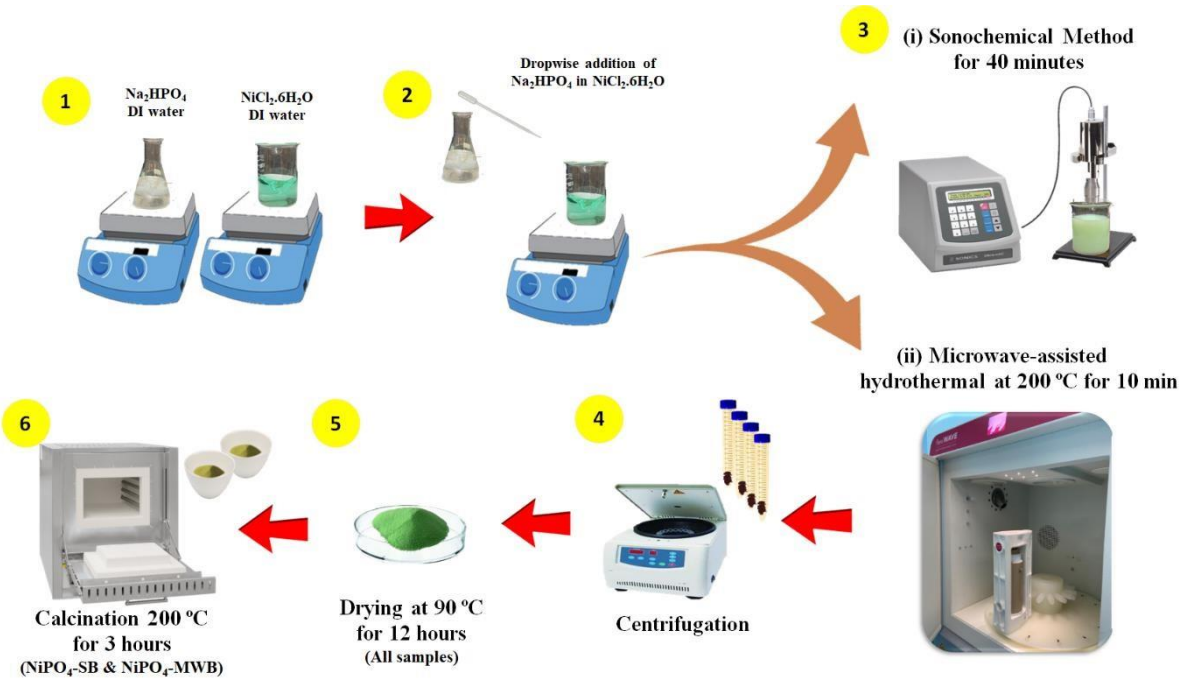

Figure 1. Illustration of the synthesis process ($Ni_3(PO_4)_2$) nanoparticles via a sonochemical and microwave-assisted hydrothermal method.

2.4 Characterization of the materials

Structural studies of the synthesized materials were performed using Fourier-transform infrared spectroscopy (FTIR) and X-Ray Diffraction (XRD) analysis. The presence of the functional groups in the synthesized materials was determined using FTIR (PerkinElmer Spectrum 400). The materials were scanned from 500 to 4000 cm^{-1} with a resolution of 1 cm^{-1} in transmittance mode. Meanwhile, the crystallinity of the synthesized materials was characterized using Rigaku

SMartLab X-ray diffractometer with Cu Kα radiation (λ = 1.5418 Å) in the 2θ range between 5° and 80° at ambient temperature. The sample's morphology was characterized using a Field Emission Scanning Electron Microscope (FEI Quanta 400F). The elemental analysis was performed using an energy-dispersive X-ray spectrometer (Oxford-instruments INCA 400) with X-Max Detector. Raman spectra were recorded using a Micro-Raman spectrometer (WITec Alpha300) under 532 nm green

laser diode excitation in 400–800 cm^{-1}. The data obtained from all the characterizations were plotted into their respective spectra using Origin 2017.

2.5 Electrode fabrication and evaluation of the electrode

A cleaned nickel foam was coated with a slurry consisting of 75:15:10 wt% of active materials: carbon black: binder (PVdF in NMP), respectively, and dried in a vacuum oven at 60 °C for 12 hours. The electrochemical studies were performed using a three-electrode system; coated nickel foam, platinum wire, and potassium chloride (KCl) saturated silver-silver chloride (Ag/AgCl) as the working, counter, and reference electrodes. Meanwhile, a standard twoelectrode system was assembled by combining the positive electrode (optimized $Ni_3(PO_4)_2$ nanoparticle electrode) and the negative electrode (activated charcoal electrode) to investigate the performance device. These electrodes were separated with filter paper. A concentrated potassium hydroxide (KOH) solution at a molarity of 1 M served as the electrolyte for the two electrode configurations under investigation. Cyclic voltammetry (CV), galvanometric chargedischarge (GCD), and electrochemical impedance spectroscopy (EIS) with a frequency range from 0.01Hz to 100 kHz were conducted using Gamry Instrument Interface 1010E potentiostatgalvanostat.

3. Results and discussion

The self-nucleation and material growth initiated the formation of $Ni_3(PO_4)_2$ nanoparticles. Upon the dissolution of $NiCl_2.6H_2O$ and Na_2HPO_4 in DI water, the precursors start to dissociate, forming ions, as explained through the following equations:

$$NiCl_2.6H_2O \rightarrow Ni^{2+} + 2Cl^- + 6H_2O \quad (1)$$

$$Na_2HPO_4 \rightarrow 2Na^+ + HPO_4^{2-} \quad (2)$$

A transparent light green solution of $NiCl_2.6H_2O$ turned into a cloudy light green colloid solution after adding Na_2HPO_4. The nucleation and growth of the nanoparticles happen once the mixture is subjected to sonochemical and microwave-assisted hydrothermal syntheses. In sonochemical

synthesis, the ultrasonic waves are absorbed by the dissociated ions and water molecules. This phenomenon then induced the acoustic cavitation phenomena in which nucleation and growth of nanoparticles happened under ultrasonic waves. Meanwhile, microwave-assisted hydrothermal uses rapid microwave heating. During the synthesis, microwave energy penetrates through the dissociated ions. These ions absorbed the microwave energy and converted it into heat energy, initiating the process of nucleation and growth of the $Ni_3(PO_4)_2$ nanoparticles[41,42]. The formation of $Ni_3(PO_4)_2$ nanoparticles in both methods is as follows:

$$3NiCl_2.6H_2O + 6Na_2HPO_4 \rightarrow Ni_3(PO_4)_2 + 6NaCl + 18H_2O + H_3PO_4 + 6Na_2HPO_4\,(excess) \quad (3)$$

3.1 Structural studies

Figure 2(a) shows the XRD patterns of the $Ni_3(PO_4)_2$ nanoparticles synthesized via sonochemical and microwave-assisted hydrothermal methods. The $NiPO_4$-SA and $NiPO_4$-SB showed similar sets of diffraction peaks located at 11.60°, 12.64°, 18.65°, 22.42°, 23.64°, 28.48°, 30.76°, 34.79°, 39.67°, 41.42°, 56.68°, and 71.59° that indicate to the (110), (020), (200), (130), (101), (031), (301), (330), (112), (341), (332) and (442) crystal planes of nickel phosphate hydrate [$Ni_3(PO_4)_2.8H_2O$], in agreement with standard (JCPDS no. 00-033-0951) values (Figure 2a) [43]. Comparing the XRD pattern of the $NiPO_4$-SA and $NiPO_4$-SB samples, it can be seen that the latter possesses less intense diffraction peaks, which denotes that the degree of crystallinity was reduced after the calcination. In the case of $NiPO_4$-SA, the asprepared sample, it initially existed as a hydrated form containing water molecules. Heat application leads to removing these water molecules, subsequently disrupting the crystal structure [44]. Consequently, the atomic arrangement within the crystal lattice of $NiPO_4$-SB undergoes rearrangement, decreasing its degree of crystallinity [45]. This phenomenon is also reflected in the colour change of the nanoparticles, whereby the light green colour of $NiPO_4$SA and $NiPO_4$-MWA indicates of hydrate nanoparticle has changed to dark off-white after calcination ($NiPO_4$-SB and $NiPO_4$-MWB). As depicted in Figure 2b, the XRD pattern of the $NiPO_4$-MWA sample did not show any diffraction peaks; instead, it only showed two broad peaks at 2θ=25° and 35°. These broad peaks confirmed the amorphous nature of $NiPO_4$-MWA samples produced through

the microwave-assisted hydrothermal method. Meanwhile, only a broad peak between 20° to 40° is observed in the XRD spectra of $NiPO_4$-MWB, corresponding to the overlapping of two peaks shown in the XRD spectra of $NiPO_4$-MWA. This is similar to $NiPO_4$-SB, where calcination removed the water molecules, reducing its degree of crystallinity (in this case, it increased the amorphous nature of the $NiPO_4$-MWB). The disordered atomic arrangement of materials provides a continuous electronic channel for charge transfer within the device and further enhances electrochemical performance during the charge/discharge process [46].

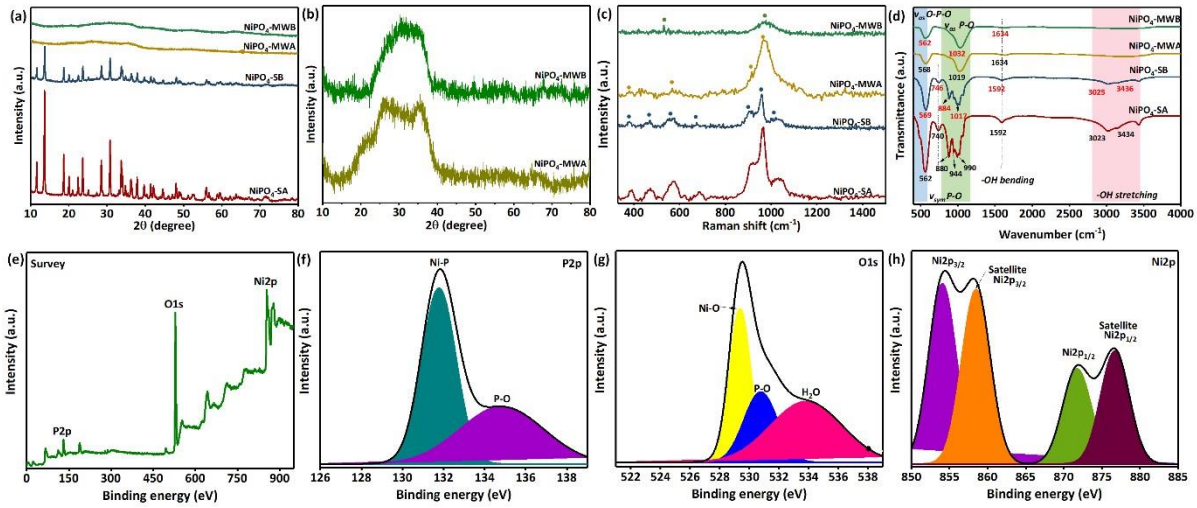

Figure 2. (a) XRD patterns of all the synthesized nickel phosphate, (b) Comparison of XRD patterns between $NiPO_4$-MWA and $NiPO_4$-MWB, (c) Raman spectra (d) FTIR of all the synthesized nickel phosphate; $NiPO_4$-SA, $NiPO_4$-SB, $NiPO_4$-MWA and $NiPO_4$-MWB, and (e-h) XPS spectra of $NiPO_4$-MWB.

The vibrational activity of chemical bonding of $NiPO_4$-SA, $NiPO_4$-SB, $NiPO_4$-MWA and $NiPO_4$-MWB samples were analyzed by Raman spectra, as shown in Figure 2c. The $NiPO_4$SA and $NiPO_4$-SB depicted three strong peaks at 1041, 962 and 922 cm^{-1}, corresponding to the v_3 asymmetric stretching mode of phosphate ligands (PO_4), v_1 mode of orthophosphate (PO_4^3), and v_1 symmetric stretching mode of PO_4, respectively [47,48]. In addition, another three characteristic peaks representing the asymmetric bending vibration of phosphate are found at 690 cm^{-1} (v_2), 472 cm^{-1} (v_2) and 389 cm^{-1} [47,49]. The peak found at 572 cm^{-1} corresponds to the Ni-O stretching mode, indicating that the synthesized nanoparticles are a nickel-containing compound. Certain phosphate peaks, specifically those at 472 and 690 cm^{-1} for $NiPO_4$-MWA, and 389, 472, 690, and 922 cm^{-1} for $NiPO_4$-

MWB, did not exhibit clear visibility in the respective spectra. This lack of distinctness is presumed to stem from alterations induced by disorder in intermolecular interactions, as noted in XRD [24]. The disordered structure of amorphous $NiPO_4$-MWA and $NiPO_4$-MWB gives rise to varying bond angles and lengths in chemical interactions with neighbouring molecules [50]. Consequently, it is difficult to detect some peaks due to the inherent insensitivity to Raman spectroscopy.

Figure 2d shows the FTIR spectra of all the synthesized samples. The analysis confirms the presence of phosphate-based nanoparticles in all the synthesized samples. Notably, distinct phosphate vibrational bands are observed in each spectrum, indicating unique chemical bonding characteristics among the synthesized samples. Among them, the characteristic peaks at 562 cm^{-1} ($NiPO_4$-SA), 569 cm^{-1} ($NiPO_4$-SB), 568 cm^{-1} ($NiPO_4$-MWA), 562 cm^{-1} ($NiPO_4$MWB) assigned to fingerprints of asymmetric deformation vibration of PO_4 in phosphate group (PO_4^{3-}) [51] or triply degenerate bending mode (v_4) of the O–P–O bond [39]. The other characteristic peaks at around ~740 cm^{-1} correspond to the P-O bond's symmetric stretching mode (v_{sym}). Meanwhile, the peaks in the range 880 – 1032 cm^{-1} are assigned to the asymmetric stretching mode (v_{as}) of the P-O bond in the PO_4^{3-} [45]. The peaks attributed to phosphate bonds, specifically those around ~740 cm^{-1} and 880-1000 cm^{-1}, were not distinctly discernible in the spectra of $NiPO_4$-MWA and $NiPO_4$-MWB. These spectra exhibit analogous characteristics to their respective Raman spectra. The diminishment of these peak intensities can be attributed to the overlap of bands and the broadening typical of their amorphous structure, which are in agreement with XRD findings [52][39]. In addition, the peaks at wavenumber around 1600 cm^{-1} in all the spectra represent the adsorption of -OH bending. The $^{-}$OH stretching is also seen at wavenumber in the 3000 – 3600 cm^{-1} range. The intensity of these peaks is gradually reduced after exposure to the calcination, as shown in the $NiPO_4$-SB and $NiPO_4$-MWB spectra (Figure 2d). This is because of the removal of water molecules from the crystal structure of $NiPO_4$-SB and $NiPO_4$-MWB upon calcination, which caused the formation of an amorphous structure. X-ray photoelectron spectroscopy (XPS) provides critical insights into the chemical composition and oxidation states in the microwave-synthesized $NiPO_4$-MWB sample. The XPS survey spectra,

depicted in Figure 2e, reveal distinct peaks corresponding to the presence of nickel (Ni), phosphate (P), and oxygen (O) elements. Further insights into the chemical bonding were obtained through high-resolution spectra, as shown in Figures 2f-h. In Figure 2f, the P2p spectrum displays discernible binding energies at 131 eV and 133 eV, corresponding to Ni-P and P-O bonds, respectively [53]. Detailed examination of the O1s spectrum in Figure 2g uncovers three distinct fitted peaks at 529 eV, 531 eV, and 534 eV, corresponding respectively to Ni-O, P-O [54], and gas phase water (H_2O) interactions [7]. The Ni2p spectrum in Figure 2h presents a prominent peak centred at 854 eV, accompanied by a satellite peak at 859 eV, attributed to $Ni2p_{3/2}$, while an additional peak centred at 872 eV, along with its satellite peak at 877 eV, corresponds to $Ni2p_{1/2}$. These well-defined XPS peaks provide compelling evidence for the presence of Ni^{2+} species within the synthesized $NiPO_4$MWB material [55,56]. Therefore, the XPS results conclusively confirm the successful formation of nickel (Ni), phosphate (P), and oxygen (O) constituents within the $NiPO_4$-MWB structure.

3.2 Morphology studies

The morphologies of $NiPO_4$-SA, $NiPO_4$-SB, $NiPO_4$-MWA and $NiPO_4$-MWB samples were revealed by employing Field Emission Scanning Electron Microscope (FESEM). Generally, sonochemical synthesis is a process that applies the concept of sonochemistry. During the sonochemical process, the molecule in the solution experience acoustic cavitation involving the bubbles' formation, growth and implosive collapse. The collapse of the bubbles creates a short-lived localized hot spot with extremely high temperature and pressure [57], which is responsible for producing the flakes-like shape of $NiPO_4$-SA and $NiPO_4$-SB samples, as shown in Figures 3a and 3b. On the other hand, the microwave-assisted hydrothermal process is a method that utilizes high temperature and sealed pressure during the process. Microwave heating creates a uniform size of $NiPO_4$-MWA and $NiPO_4$-MWB samples because it has no thermal gradients throughout the bulk solution [35]. Meanwhile, high temperature and pressure during the process create a smaller particle (as shown in Figures 3c and 3d) than the sonochemical method. Small particles allow for more electrolyte ions penetration

through the material, thus improving the electrochemical performance of the electrode. The energy dispersive X-Ray (EDX) analysis displayed in Figure 3 (e-h) confirms the presence of nickel (Ni), phosphate (P) and oxygen (O) without any other impurity in all $NiPO_4$-SA, $NiPO_4$-SB, $NiPO_4$-MWA and $NiPO_4$-MWB samples. The presence of carbon (C) element in the EDX result corresponds to the carbon tape used during the characterization. The particle produced from both methods is nickel phosphate.

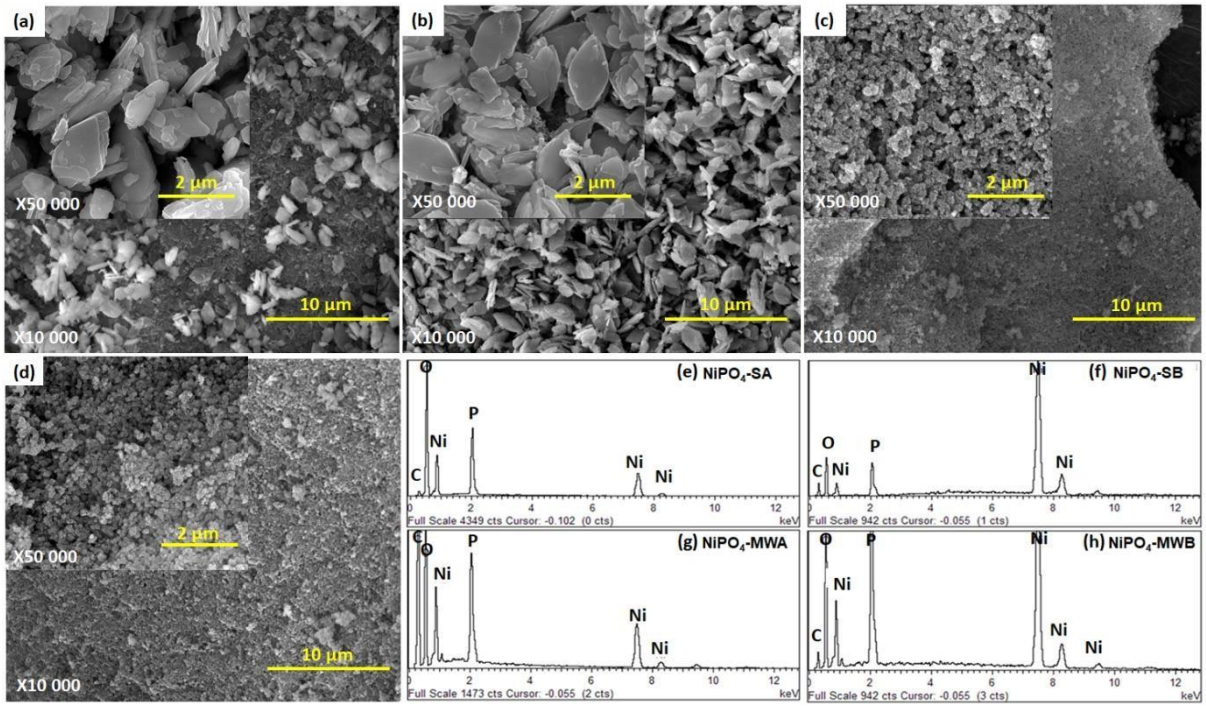

Figure 3. FESEM images of (a) $NiPO_4$-SA, (b) $NiPO_4$-SB, (c) $NiPO_4$-MWA, and (d) $NiPO_4$MWB. (e-h) EDX analysis for all the synthesis nickel phosphate particles.

3.3 Electrochemical performance of the electrode (three-electrode studies)

The CV curves for all the samples displayed well-defined redox peaks revealing the domination of diffusion-control kinetics in the electrode material (Figure 4a-d). The inherent electrochemical properties of $NiPO_4$-SA, $NiPO_4$-SB, $NiPO_4$-MWA and $NiPO_4$-MWB electrodes were analyzed in a three-electrode system using 1 M of KOH electrolyte. Figure 4ad represents the CV curves of the electrodes obtained from different scan rates from 3 to 50 mV s^{-1}. All the samples were tested at the potential range of 0 to 0.5V vs. Ag/AgCl. A pair of redox peaks (0.34 V for the oxidation peak and 0.24 V for the reduction peak) can be seen at the lowest scan rate (3 mV s^{-1}) of $NiPO_4$-SA and $NiPO_4$-

SB electrodes. Similarly, the CV curves of the $NiPO_4$-MWA and $NiPO_4$-MWB electrodes synthesized via microwave-assisted hydrothermal method showed a pair of redox peaks (Figures 4c and d). The redox peaks confirmed the battery-type behaviour of the electrodes, which store charge via reversible Faradaic reactions between Ni^{2+} and Ni^{3+} at the electrode/electrolyte interface [58]. Unlike the other electrodes, the CV of a $NiPO_4$-SB electrode shows prominent oxidation peaks splitting as the scan rate increases. The split of two oxidation peaks can be associated with chemical state changes of Ni^{2+}/ Ni^{3+}/Ni^{4+} [59,60]. This splitting also can be due to the development of highly resistant passivation layers or known as solid electrolyte interphase (SEI), affected by calcination of sonochemical $NiPO_4$-SB electrode causing high overpotentials for the oxidation of Ni^{2+} to Ni^{3+} and Ni^{3+} to Ni^{4+} [61]. It can be noticed that, as the scan rate increased, the redox peaks of all electrodes shifted to a higher potential for oxidation peaks while the lower potential for the reduction peaks. This phenomenon was due to the asynchronous movement of electrolyte ions with increasing scan rates. To further support the characteristics of the $NiPO_4$SA, $NiPO_4$-SB, $NiPO_4$-MWA and $NiPO_4$-MWB electrodes, a comparative CV curve at 3 mV/s has been shown in Figure 4e. The CV curves show different redox peaks of $NiPO_4$-MWA and $NiPO_4$-MWB electrodes compared to $NiPO_4$-SA and $NiPO_4$-SB electrodes. Electrode materials synthesized via microwave-assisted hydrothermal show a more positive oxidation peak potential; 0.43 V for $NiPO_4$-MWA and 0.45 V for $NiPO_4$-MWB. Meanwhile, the reduction peak is shown at a more negative potential of 0.22 and 0.18 V for $NiPO_4$-MWA and $NiPO_4$MWB, respectively. The change in the redox peaks $NiPO_4$-MWA and $NiPO_4$-MWB electrodes compared to their counterpart electrodes is due to its amorphous structure (as evident from the XRD result), which allows for rapid ions transportation [62] and deep intercalation of the ions in the electrode material [63,64]. The possible redox equation in all four electrode materials is as follows: $Ni_3(PO_4)_2 + 3OH^- \leftrightarrow Ni_3(OH)_3(PO_4)_2 + 3e^-$ [39].

The comparison of the area of CV curves shows that the $NiPO_4$-MWB electrode has exhibited the highest peak current and largest area under the curve, indicating excellent electrode performance, superior charge storage performance, and higher specific capacity.

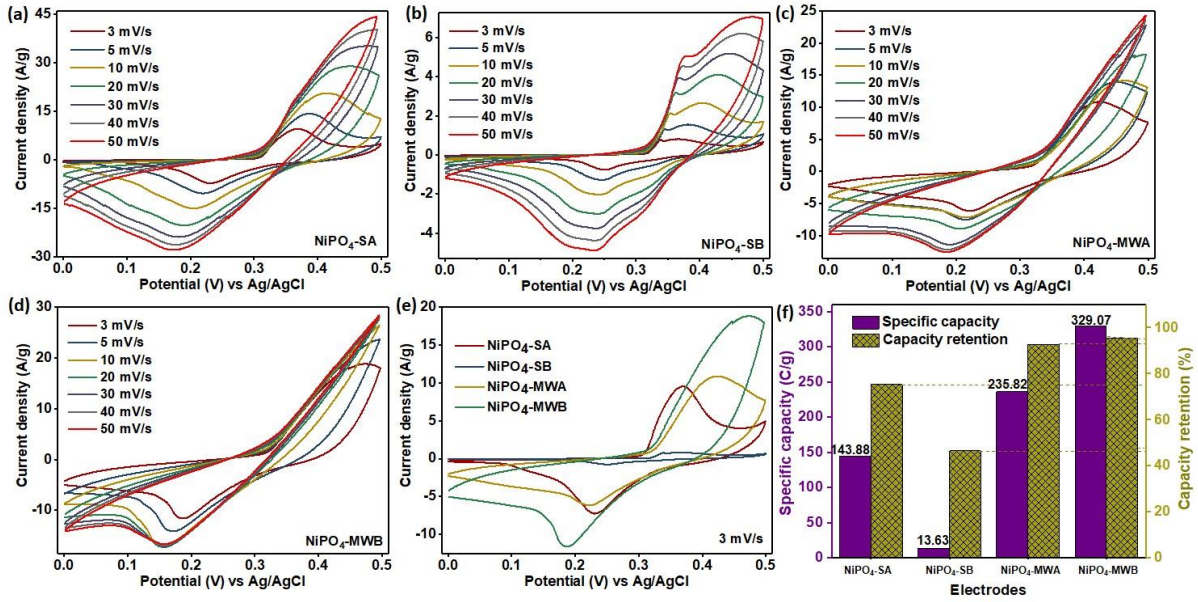

Figure 4. CV curves of (a) $NiPO_4$-SA, (b) $NiPO_4$-SB, (c) $NiPO_4$-MWA and (d) $NiPO_4$-MWB at various scan rates. Comparison of (e) CV curves, (f) specific capacity of all electrodes at the lowest scan rate of 3 mV s^{-1} and capacity retention when the scan rates reach 50 mV s^{-1}.

The specific capacity ($Q_{S,\,CV}$) of the electrodes can be calculated using the following equation:

$$Q_{S,CV} = \frac{1}{vm}\int_{Vi}^{Vf} I \times \mathrm{dV} \qquad (4)$$

Where $\int I\,dv$ represents an area under the CV curve, v is the scan rate (V s^{-1}), and m is the mass of the active material coated on the substrate (g). The maximum specific capacity that was achieved for $NiPO_4$-SA, $NiPO_4$-SB, $NiPO_4$-MWA and $NiPO_4$-MWB electrodes at 3 mV s^{-1} are 143.88, 13.63, 235.82 and 329.07 C g^{-1}, respectively. Amongst all the electrodes, the $NiPO_4$MWB electrode exhibited the highest specific capacity and good capacity retention of 95.5 %, as depicted in Figure 4f. The underlying mechanism for this performance enhancement can be attributed to the amorphous structure, which offers more exposed redox active sites for faradaic reactions, leading to the material's high performance. Meanwhile, sonochemical produced a higher degree of crystallinity of $NiPO_4$-SA and $NiPO_4$-SB, limiting the redox active side for the reaction to occur. Thus, both $NiPO_4$-SA and $NiPO_4$-SB electrodes exhibit lower specific capacity. The galvanometric charge-discharge (GCD) curves of all the electrodes at different current densities ranging from 1 to 7 A g^{-1} are depicted in Figure 5 a-d. All the electrodes show non-linear charge-discharge curves corresponding to their faradaic properties, which agrees with the CV curves. It can be noticed that the discharge time

becomes shorter as the current density increases. This trend explains the diffusion and intercalation of the ions, where a high current density reduces the diffuse and intercalate time of the ions into the active material. Meanwhile, lower current density gives the ions time to diffuse and intercalate into the active material.

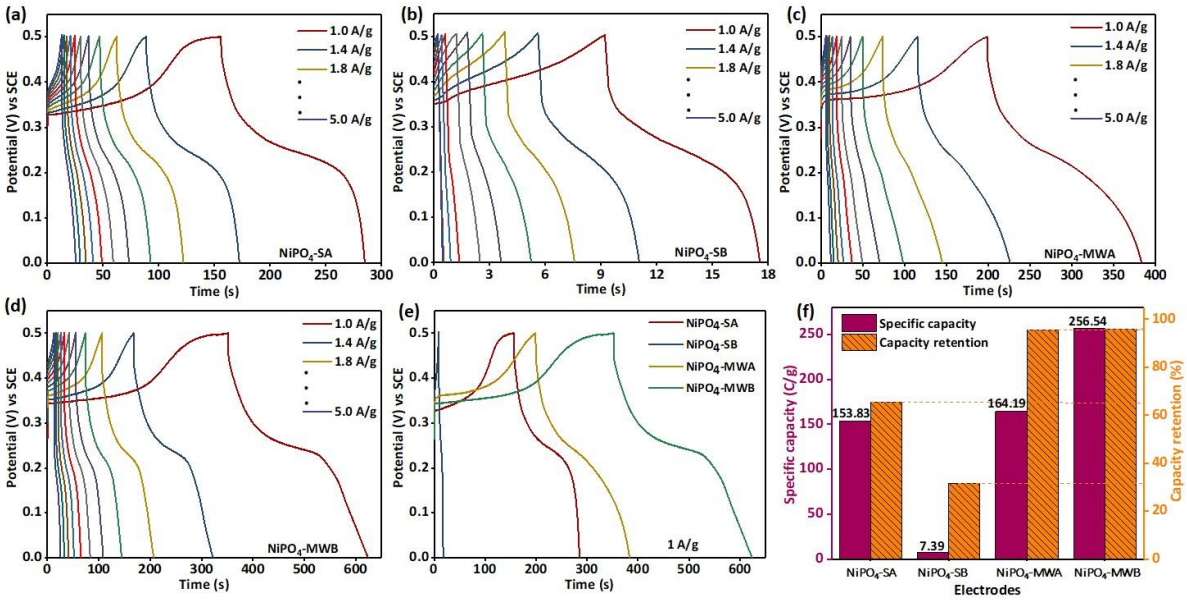

Figure 5. Galvanostatic charge-discharge (GCD) curves of (a) $NiPO_4$-SA, (b) $NiPO_4$-SB, (c) $NiPO_4$-MWA and (d) $NiPO_4$-MWB at various current densities. Comparison of (e) GCD curves, (f) specific capacity of all electrodes at 1 A g^{-1} and capacity retention when the current densities reach 5 A g^{-1}.

The GCD curves of $NiPO_4$-SA, $NiPO_4$-SB, $NiPO_4$-MWA and $NiPO_4$-MWB electrodes were collected at 1 A g^{-1} (Figure 5e). We note that the discharge time of $NiPO_4$-MWB electrodes is the longest, 271.8 s, among their counterpart electrodes, implying superb electrochemical performance. The specific capacity ($Q_{S,\,GCD}$) of the electrodes can be calculated using the following equation:

$$Q_{S,GCD} = \frac{I \times \Delta t}{m} \tag{5}$$

Where I represent the discharge current (A), Δt is the discharging time (s), and m is the mass of the active material coated on the substrate (g). The specific capacity $NiPO_4$-MWB electrode is calculated to be 256.54 C g^{-1} at a current density of 1 A g^{-1}, which is superior to other electrodes $NiPO_4$-SA (153.83 C g^{-1}), $NiPO_4$-SB (7.39 C g^{-1}), and $NiPO_4$-MWA (164.19 C g^{-1}). The outstanding electrochemical performance of the $NiPO_4$-MWB electrode is because it has the largest area under

the CV curve and a longer discharge time. In summary, $NiPO_4$-MWB is considered an optimized active material in this work due to the potential of the microwaveassisted hydrothermal approach used to produce this material able to make (i) smaller size nanoparticles and (ii) a highly amorphous nature compared to other electrode material. The small particle size of $NiPO_4$-MWB improves the electrochemical performance of the sample by providing more active sites for faradic redox reactions. Besides, smaller particle size increases the specific surface area and reduces agglomeration tendency even after calcination [38,65]. The removal of water contents from the crystal structure of $NiPO_4$-MWB led to the deformation of the crystal to form a highly amorphous nature which can also improve the electrode's electrochemical performance [66,67]. Amorphous materials' unsaturated structure provides abundant active sites for surface-based faradaic reactions [45]. At the same time, the disordered atomic arrangement affords a continuous pathway for charge transportation during the charge/discharge process [67].

3.4 Supercapattery assembly and electrochemical characterization (two-electrode studies)

Two-electrode studies were carried out on the optimized battery-type electrode ($NiPO_4$-MWB) to investigate its capability in supercapattery further. It was treated as positive, while the AC capacitive electrode was negative. Before CV and GCD testing, charge balancing on both $NiPO_4$-MWB and AC electrodes was done by using the following equation:

$$\frac{Q_{S-}}{Q_{S+}} = \frac{m_+}{m_-} \quad (6)$$

where m_+ and m_- are the mass loading of $NiPO_4$-MWB and AC electrodes, respectively. Q_{S+} and Q_{S-} are the specific capacities of $NiPO_4$-MWB and AC electrodes, respectively. Figure 6a displayed the CV patterns of the individual $NiPO_4$-MWB and AC electrodes at a scan rate of 10 mV s^{-1} and a potential window range of 0 - 0.5 and -1 - 0 V, respectively. It can be observed that the AC electrodes behave as capacitive-type electrodes, as evidenced by the rectangular CV curve. The CV curves of the full-cell ($NiPO_4$-MWB//AC) were plotted in Figure 6b. It was tested at a potential window of 1.5 V with different scan rates ranging from 10 to 100 mV s^{-1}. The CV curves showed that the assembled

$NiPO_4$-MWB//AC displayed a combination of rectangular CV curves without a redox peak at the lower potential window of 0-0.5V and a rectangular CV curve with a redox peak at a higher potential window of 0.6-1.5V. This situation ascribed that the Faradaic reaction and the electric double-layer formation contributed to the energy storage of the assembled $NiPO_4$-MWB//AC. The symmetrical nature of all GCD curves at different current densities of 1 to 5 A g^{-1} is shown in Figure 6c. The GCD curves depicted the charge storage mechanisms of the supercapattery, which combined the capacitive-type (electric double layer formation) and battery-type (faradaic reaction) electrodes. The GCD results are in agreement with the CV results of the $NiPO_4$-MWB//AC. The curves reveal that the $NiPO_4$-MWB//AC has good electrochemical reversibility with a specific capacity of 49.6 C g^{-1} at 1 A g^{-1}. It is noticeable that it can sustain up to 50.6 % capacity retention when the current density reaches 5 A g^{-1} with a specific capacity of 24.5 C g^{-1}. The energy density and power density are important indicators for the $NiPO_4$-MWB//AC. It delivers a high energy density of 10.33 Wh kg^{-1} at a power density of 750 W kg^{-1} upon being charged up to 1.5 V. The remarkable value of energy and power densities of the assembled $NiPO_4$-MWB//AC is comparable with the literature on nickel-based phosphate nanoparticles, as shown in the Ragone plot (Figure 6d) and summarised in Table 1. It is acknowledged that other studies have reported even higher energy densities—such as NiCoP (42.25 Wh/kg) [68] and $NiCo(PO_4)_3$ (32 Wh/kg) [69]. These superior energy densities are attributed to incorporating bimetallic phosphate materials, combining nickel and cobalt, which inherently generate more redox active sites, thereby augmenting electrical charge storage capacity.

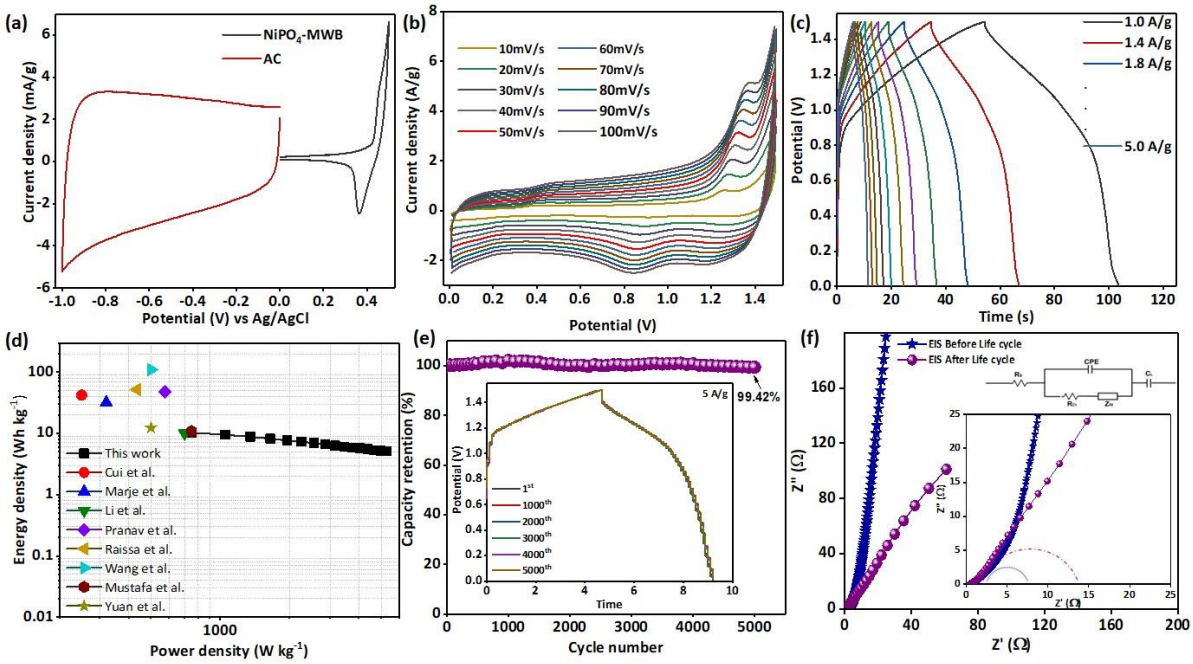

Figure 6. (a) CV curves of the activated charcoal and $NiPO_4$-MWB electrodes tested in a three-electrode system, (b) CV curves of the asymmetric supercapacitor of $NiPO_4$-MWB//AC at various scan rates, (c) GCD curves of $NiPO_4$-MWB//AC at various current densities, (d) Ragone plot, (e) cyclic performance and (f) Nyquist plots of the $NiPO_4$-MWB//AC at 0^{th} and after $5{,}000^{th}$ cycles.

Table 1. Comparison of the energy density, power density and stability of the assembled $NiPO_4$-MWB//AC with other reported nickel nanoparticle-based energy storage.

Material	**Energy density (Wh/kg)**	**Power density (W/kg)**	**Stability**	**Ref**
$Ni_3(PO_4)_2$	10.33	750	99.42% (5000 cycles)	This work
NiCoP	42.25	250	82.84% (8000 cycles)	[68]
$NiCo(PO_4)_3$	32	320	89%	[69]
NiMnO	10	700	-	[70]
Ni_3S_2	7.6	600	95.59% (2000 cycles)	[71]
NiP-600	52	434	71% (2000 cycles)	[72]
NiCoP	10.88	750	70% (5000 cycles)	[73]
ACG-N-P-Ni	12.32	499.99	92.6% (3000 cycles)	[56]

In contrast, our study adopts a distinct approach by employing microwave-assisted hydrothermal synthesis to produce nickel phosphate nanoparticles. This strategy accelerates reaction kinetics,

reduces synthesis time compared to sonochemical methods, and introduces an essential facet of stability enhancement compared to other reported work. As indicated in Figure 6e, our device ($NiPO_4$-MWB//AC) exhibits remarkable stability even after undergoing 5000 cycles. It can be noticed that the capacity retention increased to 1.9 % starting from cycle 0^{th} to 1300^{th} due to the device being in activation mode. Beyond that cycle, the device decayed gradually to 99.42 % after 5000 cycles. Electrochemical impedance spectroscopy (EIS) ranging from 0.1 to 100 kHz was used to understand the internal resistance of the $NiPO_4$-MWB//AC. Figure 6f shows a Nyquist plot of $NiPO_4$-MWB//AC, taken before and after $5{,}000^{th}$ of the life cycle. The equivalent circuit model (inset Figure 6f) is used to fit the EIS data composed of equivalent series resistance (R_s), which recognizes due to the internal resistance of the device or circuit connections [74]. The diameter and shape of the semicircle of the Nyquist plot are represented by charge transfer resistance (R_{ct}) and constant phase angle (CPE), respectively.

R_{ct} explained the internal charge transfer resistance at the electrode and electrolyte interface. The Nyquist plot of the 0th cycle shows the spike's semicircle and a steep slope at high and low frequencies, respectively. The spike indicates the device's capacitive-like behaviour, represented by the Warburg impedance (Z_w). C_L is the limit capacitance in the circuit. After the $5{,}000^{th}$ cycle, a semicircle with R_{ct} value of 16.9 Ω and a gradual slope of the spike was seen. The results from the decay of electrochemical performance agree with the capacity retention of the device after the $5{,}000^{th}$ cycle [75,76].

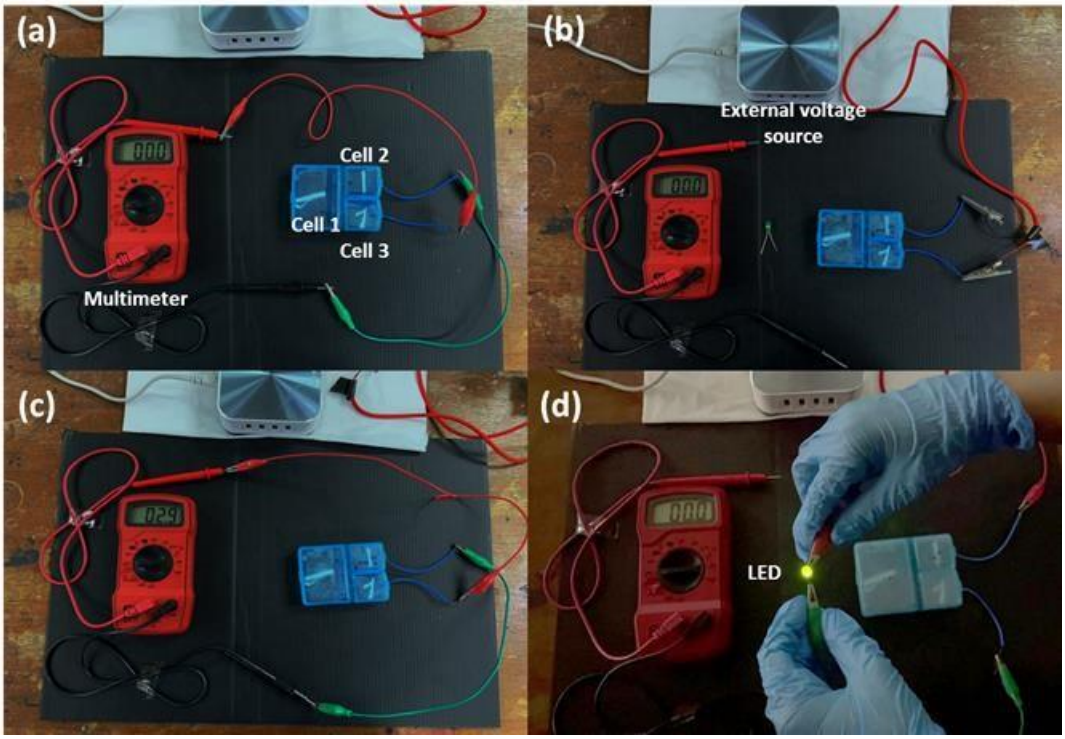

Figure 7. (a) Initial voltage stored by three sets of $NiPO_4$-MWB//AC supercapattery connected in series, (b) charging of the fabricated device via an externally applied voltage source, (c) voltage stored after charging and (d) illuminating a green LED.

The practical application of the optimized supercapattery was demonstrated through the lighting up of green LED light, as illustrated in Figure 7a-d. Three sets of optimized supercapattery units (2.5 cm x 2.5 cm), configured as NiPO4-MWB//AC, were fabricated. These electrode assemblies were effectively separated by filter paper, connected in series, and placed in a container. Following the cells' sequential assembly connection, a solution of KOH electrolyte was inserted into the container, resulting in an initial stored voltage reading of 0 V (Figure 7a), indicating the uncharged state of the device. Then, the device was charged up via an externally applied voltage source (Figure 7b) for 3 minutes. With the completion of the charging process, the external voltage source was removed, and the charged voltage was recorded to be 2.9 V (Figure 7c). Then, the devices are connected with a green light-emitting diode (LED). The device successfully to powered up the LED for approximately 2 minutes before gradually fading. The device's charging and discharge were repeated and showed consistent performance.

4. Conclusion

In this study, we have successfully utilized two distinct methods to fabricate nickel phosphate ($Ni_3(PO_4)_2$) nanoparticles with diverse structural and morphological properties. Sonochemical approaches produced $NiPO_4$-SA and $NiPO_4$-SB electrode materials with flake-like and crystalline structures, respectively. In contrast, microwave-assisted hydrothermal processes resulted in smaller-sized $NiPO_4$-MWA and $NiPO_4$-MWB electrode materials with amorphous structures. Among all samples, $NiPO_4$-MWB was selected as the optimized electrode material owing to its superior specific capacity. This result is attributed to its small size, which permits increased ion penetration into the interior surface of the electrode material. Additionally, the disordered arrangement of $NiPO_4$-MWB facilitates deep intercalation of ions in the electrode material. It was then used as a positive electrode in the supercapattery using a standard 1M KOH electrolyte. The assembled $NiPO_4$-MWB//AC delivers a maximum energy density of 10.33 Wh kg^{-1} at a power density of 750 W kg^{-1}. The capacity retention is 99.42 % after the 5,000th cycle. The electrochemical studies of CV and GCD depicted the charge storage mechanisms of the supercapattery, which combined the capacitive-type (electric double layer formation) and battery-type (faradaic reaction) electrodes.

Acknowledgement

The authors would like to acknowledge the funding support under Sunway University Internal Grant Scheme (GRTIN-IGS-GAMRG[S]-13-2022).

References

[1] L. Zhang, X. Hu, Z. Wang, F. Sun, D.G. Dorrell, A review of supercapacitor modeling, estimation, and applications: A control/management perspective, Renew. Sustain. Energy Rev. 81 (2018) 1868–1878. https://doi.org/10.1016/j.rser.2017.05.283.

[2] P. Sun, X. Zhang, S. Wang, Y. Zhu, Lithium-ion battery degradation caused by overcharing at low temperatures, Therm. Sci. Eng. Prog. 30 (2022) 101266.

[3] J. Liu, Q. Duan, W. Peng, L. Feng, M. Ma, S. Hu, J. Sun, Q. Wang, Slight overcharging cycling failure of commercial lithium-ion battery induced by the jelly roll destruction, Process Saf. Environ. Prot. 160 (2022) 695–703.

[4] S.Y. Poy, S. Bashir, F.S. Omar, N.M. Saidi, N.K. Farhana, V. Sundararajan, K. Ramesh, S. Ramesh, Poly (1-vinylpyrrolidone-co-vinyl acetate) (PVP-co-VAc) based gel polymer electrolytes for electric double layer capacitors (EDLC), J. Polym. Res. 27 (2020) 1–10. https://doi.org/10.1007/s10965-020-2016-x.

[5] K.H. Guan, N.K. Farhana, F.S. Omar, N.M. Saidi, S. Bashir, S. Ramesh, K. Ramesh, Influence of tetraglyme towards magnesium salt dissociation in solid polymer electrolyte for electric double layer capacitor, J. Polym. Res. 27 (2020). https://doi.org/10.1007/s10965-020-02070-z.

[6] F. Ramlee, N.K. Farhana, S. Bashir, N.M. Saidi, F.S. Omar, S. Ramesh, K. Ramesh, S. Ramesh, Electrical property enhancement of poly (vinyl alcohol-co-ethylene)–based gel polymer electrolyte incorporated with triglyme for electric double-layer capacitors (EDLCs), Ionics (Kiel). 27 (2021) 361–373. https://doi.org/10.1007/s11581-02003787-z.

[7] O. Gerard, A. Numan, M.A.A.M. Abdah, M. Khalid, S. Ramesh, K. Ramesh, Rapid synthesis of nikel-copper phosphate electrode by microwave-assited hydrothermal reaction for supercapattery, J. Energy Storage. 61 (2023) 106813.

[8] F.M. Aris, M. Pershaanaa, S. Gunalan, S. Bashir, F. Saiha Omar, N.M. Saidi, K. Ramesh, S. Ramesh, Surface modification of metal phosphate Binder-Free electrode with metal hydroxides for supercapattery, FlatChem. 39 (2023). https://doi.org/10.1016/j.flatc.2023.100504.

[9] B. Akinwolemiwa, G.Z. Chen, Fundamental consideration for electrochemical engineering of supercapattery, J. Braz. Chem. Soc. 29 (2018) 960–972. https://doi.org/10.21577/0103-5053.20180010.

[10] L. Yu, G.Z. Chen, Ionic liquid-based electrolytes for supercapacitor and supercapattery, Front. Chem. 7 (2019) 1–15. https://doi.org/10.3389/fchem.2019.00272.

[11] N. Villanueva, C. Alegre, J. Rubin, H.A. Figueredo-Rodríguez, R.D. McKerracher, C.P. De León, M.J. Lázaro, Iron Electrodes Based on Sulfur-Modified Iron Oxides with Enhanced Stability for Iron-Air Batteries, ACS Appl. Energy Mater. 5 (2022) 13439–13451. https://doi.org/10.1021/acsaem.2c02123.

[12] R.D. McKerracher, H.A. Figueredo-Rodriguez, K. Dimogiannis, C. Alegre, N.I. Villanueva-Martinez, M.J. Lázaro, V. Baglio, A.S. Aricò, C. Ponce de León, Effect of 1-octanethiol as an electrolyte additive on the performance of the iron-air battery electrodes, J. Solid State Electrochem. 25 (2021) 225–230. https://doi.org/10.1007/s10008-020-04738-4.

[13] S. Najib, E. Erdem, Current progress achieved in novel materials for supercapacitor electrodes: Mini review, Nanoscale Adv. 1 (2019) 2817–2827. https://doi.org/10.1039/c9na00345b.

[14] C.. Sandhya, E. Rishad Baig, S. Pillai, C. Molji, A. Aravind, S.J. Devaki, Polyanilinecobalt oxide nano shrubs based electrodes for supercapacitors with enhanced electrochemical performance, Electrochim. Acta. 324 (2019). https://doi.org/10.1016/j.electacta.2019.134876.

[15] R.S. Kate, S.A. Khalate, R.J. Deokate, Overview of nanostructured metal oxides and pure nickel oxide (NiO) electrodes for supercapacitors: A review, J. Alloys Compd. 734 (2018) 89–111. https://doi.org/10.1016/j.jallcom.2017.10.262.

[16] J.N. Lacerda, D.F. Franceschini, E.A. Ponzio, L.M. Esteves, R.B. Guimarães, Y.T. Xing, Manganese oxide nanofoam prepared by pulsed laser deposition for high performance supercapacitor electrodes, Mater. Chem. Phys. 242 (2020).

https://doi.org/10.1016/j.matchemphys.2019.122459.

[17] H. Liu, Z. Liang, S. Liu, L. Zhang, H. Xia, W. Xie, Nickel Manganese Hydroxides with Thin-layer Nanosheets and Multivalences for High-performance Supercapacitor, Results Phys. 16 (2020) 102831.

[18] T.N. Ramesh, P.V. Kamath, Bi2O3 modified cobalt hydroxide as an electrode for alkaline batteries, Electrochim. Acta. 53 (2008) 4721–4726. https://doi.org/10.1016/j.electacta.2008.01.098.

[19] B.R. Wiston, M. Ashok, Electrochemical performance of hydrothermally synthesized flower-like α-nickel hydroxide, Vacuum. 160 (2019) 12–17. https://doi.org/10.1016/j.vacuum.2018.11.014.

[20] J.J. Cheng, Y. Ou, J.T. Zhu, H.J. Song, Y. Pan, Nickel sulfide cathode for stable charge-discharge rates in lithium rechargeable battery, Mater. Chem. Phys. 231 (2019) 131–137. https://doi.org/10.1016/j.matchemphys.2019.04.024.

[21] Y. Liu, S. Guo, W. Zhang, W. Kong, Z. Wang, W. Yan, H. Fan, X. Hao, G. Guan, Three-dimensional interconnected cobalt sulfide foam: Controllable synthesis and application in supercapacitor, Electrochim. Acta. 317 (2019) 551–561. https://doi.org/10.1016/j.electacta.2019.05.121.

[22] S.S. Sankar, A. Rathishkumar, K. Geetha, S. Kundu, A Simple Route for the Synthesis of Cobalt Phosphate Nanoparticles for Electrocatalytic Water Oxidation in Alkaline Medium, Energy and Fuels. 34 (2020) 12891–12899. https://doi.org/10.1021/acs.energyfuels.0c02809.

[23] B. Li, H. Pang, H. Xue, Fe-based phosphate nanostructures for supercapacitors, Chinese Chem. Lett. 32 (2021) 885–889. https://doi.org/10.1016/j.cclet.2020.07.004.

[24] X. Song, L. Gao, Y. Li, W. Chen, L. Mao, J.H. Yang, Nickel phosphate-based materials with excellent durability for urea electro-oxidation, Electrochim. Acta. 251 (2017) 284–292. https://doi.org/10.1016/j.electacta.2017.08.117.

[25] C. Liu, Y. Wang, J. Sun, A. Chen, A Review on Applications of Layered Phosphorus in Energy Storage, Trans. Tianjin Univ. 26 (2020) 104–126. https://doi.org/10.1007/s12209-019-00230-x.

[26] W. Raza, F. Ali, N. Raza, Y. Luo, K.H. Kim, J. Yang, S. Kumar, A. Mehmood, E.E. Kwon, Recent advancements in supercapacitor technology, Nano Energy. 52 (2018) 441–473. https://doi.org/10.1016/j.nanoen.2018.08.013.

[27] B.A. Mahmoud, A.A. Mirghni, K.O. Oyedotun, D. Momodu, O. Fasakin, N. Manyala, Synthesis of cobalt phosphate-graphene foam material via co-precipitation approach for a positive electrode of an asymmetric supercapacitors device, J. Alloys Compd. 818 (2020) 153332.

[28] F. Askari, E. Ghasemi, B. Ramezanzadeh, M. Mahdavian, Synthesis and characterization of the fourth generation of zinc phosphate pigment in the presence of benzotriazole, Dye. 124 (2016) 18–26.

[29] A.A. Yadav, Y.M. Hunge, S.B. Kulkarni, Synthesis of multifunctional FeCo2O4 electrode using ultrasonic treatment for photocatalysis and energy storage applications, Ultrason. - Sonochemistry. 58 (2019) 104663.

[30] R. Hamidi, S. Ghasemi, S.R. Hosseini, Ultrasonic assited synthesis of Ni3(VO4)2reduced graphene oxide nanocomposite for potential use in electrochemical energy storage, Ultrason. - Sonochemistry. 62 (2020) 104869.

[31] C.Y. Tan, F.S. Omar, N.M. Saidi, N.K. Farhana, S. Ramesh, K. Ramesh, Optimization of poly(vinyl alcohol-co-ethylene)-based gel polymer electrolyte containing nickel phosphate nanoparticles for dye-sensitized solar cell application, Sol. Energy. 178 (2019) 231–240. https://doi.org/10.1016/j.solener.2018.12.043.

[32] A.A. Yadav, Y.M. Hunge, S. Liu, S.B. Kulkarni, Ultrasound assisted growth of NiCo2O4@carbon cloth for high energy storage device application, Ultrason. - Sonochemistry. 56 (2019) 290–296.

[33] M. Guo, S. Wang, L. Zhao, Z. Gio, High performance asymmetric supercapacitor based on flowery nickel-zinc phosphate microspheres with carbon dots, Electrochim. Acta. 292 (2018) 299–308.

[34] K.V. Sankar, S.C. Lee, Y. Seo, C. Ray, S. Liu, A. Kundu, S.C. Jun, Binder-free cobalt phosphate one-dimensional nanograsses as ultrahigh-performance cathode material for hybrid supercapacitor applications, J. Power Sources. 373 (2018) 211–219.

[35] Z.Y. Cai, F. Peng, Y.P. Zi, F. Chen, Q.R. Qian, Microwave-assisted hydrothermal rapid synthesis of calcium phosphates: Structural control and application in protein adsorption, Nanomaterials. 5 (2015) 1284–1296. https://doi.org/10.3390/nano5031284.

[36] F.H. Ali, D.B. Alwan, Effect of particle size of TiO2 and additive materials to improve dye sensitized solar cells efficiency, J. Phys. Conf. Ser. 1003 (2018) 012077. https://doi.org/10.1088/1742-6596/1003/1/012077.

[37] L. Saleh Ghadimi, N. Arsalani, I. Ahadzadeh, A. Hajalilou, E. Abouzari-Lotf, Effect of synthesis route on the electrochemical performance of CoMnFeO4 nanoparticles as a novel supercapacitor electrode material, Appl. Surf. Sci. 494 (2019) 440–451. https://doi.org/10.1016/j.apsusc.2019.07.183.

[38] N.M. Saidi, F.S. Omar, A. Numan, D.C. Apperley, M.M. Algaradah, R. Kasi, A.J. Avestro, R.T. Subramaniam, Enhancing the Efficiency of a Dye-Sensitized Solar Cell Based on a Metal Oxide Nanocomposite Gel Polymer Electrolyte, ACS Appl. Mater. Interfaces. 11 (2019) 30185–30196. https://doi.org/10.1021/acsami.9b07062.

[39] F.S. Omar, A. Numan, N. Duraisamy, S. Bashir, K. Ramesh, S. Ramesh, Ultrahigh capacitance of amorphous nickel phosphate for asymmetric supercapacitor applications, RSC Adv. 6 (2016) 76298–76306. https://doi.org/10.1039/c6ra15111f.

[40] O. Gerard, A. Numan, M. Khalid, S. Ramesh, K. Ramesh, Fabrication of binder-free nickel-manganese phosphate battery-type electrode by microwave-assisted hydrothermal technique, J. Alloys Compd. 941 (2023) 168878.

[41] D.C. Onwudiwe, Microwave-assisted synthesis of PbS nanostructures, Heliyon. 5 (2019). https://doi.org/10.1016/j.heliyon.2019.e01413.

[42] H. Barani, B. Mahltig, Microwave-Assisted Synthesis of Silver Nanoparticles: Effect of Reaction Temperature and Precursor Concentration on Fluorescent Property, J. Clust. Sci. 33 (2022) 101–111. https://doi.org/10.1007/s10876-020-01945-x.

[43] S.S. Pujari, S.A. Kadam, Y.R. Ma, S.A. Khalate, P.K. Katkar, S.J. Marje, U.M. Patil, Highly sensitive hydrothermally prepared nickel phosphate electrocatalyst as nonenzymatic glucose sensing electrode, J. Porous Mater. 28 (2021) 369–381. https://doi.org/10.1007/s10934-020-01000-0.

[44] S. Krause, V. Bon, H. Du, R.E. Dunin-Borkowski, U. Stoeck, I. Senkovska, S. Kaskel, The impact of crystal size and temperature on the adsorption-induced flexibility of the Zr-based metal-organic framework DUT-98, Beilstein J. Nanotechnol. 10 (2019) 1737–1744. https://doi.org/10.3762/bjnano.10.169.

[45] A. Numan, J. Iqbal, P. Jagadish, S.G. Krishnan, M. Khalid, M. Pannipara, S. Wageh, Tailoring crystallinity of 2D cobalt phosphate to introduce pseudocapacitive behavior, J. Energy Storage. 54 (2022) 105371.

[46] Q. Li, Y. Xu, S. Zheng, X. Guo, H. Xue, H. Pang, Recent Progress in Some Amorphous Materials for Supercapacitors, Small. 14 (2018) 1–19. https://doi.org/10.1002/smll.201800426.

[47] R. Ramakrishnaiah, G.U. Rehman, S. Basavarajappa, A.A. Al Khuraif, B.H. Durgesh, A.S. Khan, I.U. Rehman, Applications of Raman spectroscopy in dentistry: Analysis of tooth structure, Appl. Spectrosc. Rev. 50 (2015) 332–350. https://doi.org/10.1080/05704928.2014.986734.

[48] J. Qi, Y. Lin, D. Chen, T. Zhou, W. Zhang, R. Cao, Autologous Cobalt Phosphates with Modulated Coordination Sites for Electrocatalytic Water Oxidation, Angew. Chemie. 132 (2020) 9002–9006. https://doi.org/10.1002/ange.202001737.

[49] J.D. Wang, D. Li, J.K. Liu, X.H. Yang, J.L. He, Y. Lu, One-Step Preparation and Characterization of Zinc Phosphate Nanocrystals with Modified Surface, Soft Nanosci. Lett. 01 (2011) 81–85. https://doi.org/10.4236/snl.2011.13015.

[50] D. Tuschel, Why are the Raman spectra of crystalline and amorphous solids different?, Spectroscopy. 32 (2017) 26–33.

[51] H. Yan, L. Wei, B. Xu, The influence of KH-550 on properties of ammonium polyphosphate and polypropylene flame retardant composites, Polym. Degrad. Stab. 96 (2011) 1382–1388. https://doi.org/10.1016/j.polymdegradstab.2011.03.016.

[52] C. Combes, C. Rey, Amorphous calcium phosphates: Synthesis, properties and uses in biomaterials, Acta Biomater. 6 (2010) 3362–3378. https://doi.org/10.1016/j.actbio.2010.02.017.

[53] R. Li, C. Liu, P. Tang, B. Yang, X. Li, G. Yang, L. Xie, NiCoP nanowire arrays embedded in 3D integrated N-doped carbon network for enhanced electrochemical oxygen evolution, Vacuum. 192 (2021) 1–8. https://doi.org/10.1016/j.vacuum.2021.110395.

[54] A.A. Mirghni, M.J. Madito, K.O. Oyedotun, T.M. Masikhwa, N.M. Ndiaye, S.J. Ray, N. Manyala, A high energy density asymmetric supercapacitor utilizing a nickel phosphate/graphene foam composite as the cathode and carbonized iron cations adsorbed onto polyaniline as the anode, RSC Adv. 8 (2018) 11608–11621. https://doi.org/10.1039/c7ra12028a.

[55] N. Parveen, M. Hilal, J.I. Han, Newly Design Porous/Sponge Red Phosphorus@Graphene and Highly Conductive Ni2P Electrode for Asymmetric Solid State Supercapacitive Device With Excellent Performance, Nano-Micro Lett. 12 (2020). https://doi.org/10.1007/s40820-019-0360-3.

[56] Z. Yuan, Y. Ma, P. Zhang, M. Zhai, C. Qin, X. Jiang, N-, P-, and Ni-Co-doped Porous Carbon from Poplar Powder and Graphene Oxide Composites as Electrode Materials for Supercapacitors, Energy and Fuels. 37 (2023) 2420–2430.

https://doi.org/10.1021/acs.energyfuels.2c03883.

[57] H. Xu, B.W. Zeiger, K.S. Suslick, Sonochemical synthesis of nanomaterials, Chem. Soc. Rev. 42 (2013) 2555–2567. https://doi.org/10.1039/c2cs35282f.

[58] Q. Zhou, Y. Gong, J. Lin, Low temperature synthesis of sponge-like NiV2O5/C composite by calcining Ni-V-based coordinatioon polymer for supercapacitor application, J. Electroanal. Chem. 823 (2018) 80–91.

[59] S. Chong, Y. Liu, W. Yan, Y. Chen, Effect of valence states of Ni and Mn on the structural and electrochemical properties of Li1.2NixMn0.8-xO2 cathode materials for lithium-ion batteries, RSC Adv. 6 (2016) 53662–53668.
https://doi.org/10.1039/c6ra09454f.

[60] K.O. Oyedotun, T.M. Masikhwa, A.A. Mirghni, B.K. Mutuma, N. Manyala, Electrochemical properties of asymmetric supercapacitor based on optimized carbonbased nickel-cobalt-manganese ternary hydroxide and sulphur-doped carbonized ironpolyaniline electrodes, Electrochim. Acta. 334 (2020).
https://doi.org/10.1016/j.electacta.2020.135610.

[61] C. Yan, X. Yang, H. Zhao, H. Zhong, G. Ma, Y. Qi, B.E. Koel, Y. Ju, Controlled Dydoping to nickel-rich cathode materials in high temperature aerosol synthesis, Proc. Combust. Inst. 38 (2021) 6623–6630. https://doi.org/10.1016/j.proci.2020.06.332.

[62] C. Mun, C.V. V Muralee, R. Vinodh, S. Sambasivam, I.M. Obaidat, H. Kim, Micro fl ower-like nickel sul fi de-lead sul fi de hierarchical composites as binder-free electrodes for high-performance supercapacitors, J. Energy Storage. 26 (2019).

[63] Z. Yan, L. Jiang, D. Chen, B. Huo, H. Zhou, Z. Huang, Nitrogen doped carbon nanotubes supported Co9S8 nanoparticles for lithium-ion batteries with excellent electrochemical performance, Mater. Lett. 282 (2021) 128850.

[64] M.A.A.M. Abdah, M. Mokhtar, L.T. Khoon, K. Sopian, N.A. Dzulkurnain, A. Ahmad, Y. Sulaiman, F. Bella, M.S. Su'ait, Synthesis and electrochemical characterizations of poly(3,4-

ethylenedioxythiophene/manganese oxide coated on porous carbon nanofibers as a potential anode for lithium-ion batteries, Energy Reports. 7 (2021) 8677–8687.

[65] W. Zhou, X. Yan, W. Zhang, Y. Li, Y. Zhu, M. Zhang, W. Zhu, X. Cheng, Tailored synthesis of nano-corals nickel-vanadium layered double hydroxide@Co2NiO4 on nickel foam for a novel hybrid supercapacitor, J. Energy Storage. 38 (2021). https://doi.org/10.1016/j.est.2021.102584.

[66] T. Wang, Y. Wang, J. Lei, R. Liu, K.J. Chen, Metal-organic framework derived directional growth of ultrathin amorphous NiCo hydroxide nanosheets on NiCo2O4 nanowire arrays for enhanced electrochemical properties, Ceram. Int. 46 (2020) 22934–22943. https://doi.org/10.1016/j.ceramint.2020.06.067.

[67] E. Niknam, H. Naffakah-Moosavy, S.E. Moosavifard, M.G. Afshar, Amorphous Vdoped Co3S4 yolk-shell hollow spheres derived from metal-organic framework for high-performance asymmetric supercapacitors, J. Alloys Compd. 895 (2005) 162720. https://doi.org/10.1016/j.jallcom.2005.05.002.

[68] M. Cui, Y. Jiang, Z. Wang, X. Wang, H. Wang, R. Wang, Roughening the surface of porous NiCoP rod-like arrays via the in situ growth of NiCoP4O12 nanoislands enables highly efficient energy storage, Dalt. Trans. (2020) 1–6.

[69] S.J. Marje, S.S. Pujari, S.A. Khalate, V. V Patil, V.G. Parale, T. Kim, H. Park, J.L. Gunjakar, C.D. Lokhande, U.M. Patil, Intercalation-type pseudocapacitive clustered nanoparticles of nickel-cobalt phosphate thin films synthesized via electrodeposition as cathode for high-performance hybrid supercapacitor devices, J. Mater. Chem. A. 1 (2022) 1–6.

[70] N.P. based materials for high-performance supercapacitors Metal (M=Co, Inorganic Chemistry Frontiers, Inorg. Chem. (2018) 11–28.

[71] R. Li, S. Wang, J. Wang, Z. Huang, Ni3S2@CoS core-shell nano-triangular pyramid arrays on Ni foam for high-performance supercapacitors, Phys. Chem. Chem. Phys. (2015) 3–7.

[72] Raissa, N.L.W. Septiani, S. Wustoni, F. Failamani, M. Iqbal, Nugraha, V. Suendo, B. Yuliarto, Improving capacity of nickel phosphate Versailles Santa Barbara-5 with calcination for high-performance asymmetric supercapacitors, J. Energy Storage. 56 (2022). https://doi.org/10.1016/j.est.2022.106109.

[73] M.N. Mustafa, M.A.A.M. Abdah, A. Numan, Y. Sulaiman, R. Walvekar, M. Khalid, Specific capacity optimization of nickel cobalt phosphate using response surface methodology for enhanced electrochromic energy storage performance, Electrochim. Acta. 441 (2023). https://doi.org/10.1016/j.electacta.2022.141765.

[74] F.S. Omar, A. Numan, S. Bashir, N. Duraisamy, R. Vikneswaran, Y.L. Loo, K. Ramesh, S. Ramesh, Enhancing rate capability of amorphous nickel phosphate supercapattery electrode via composition with crystalline silver phosphate, Electrochim. Acta. 273 (2018) 216–228. https://doi.org/10.1016/j.electacta.2018.03.136.

[75] L. Liao, A. Zhang, K. Zheng, R. Liu, Y. Cheng, L. Wang, A. Li, J. Liu, Fabrication of Cobaltous Sulfide Nanoparticle-Modified 3D MXene/Carbon Foam Hybrid Aerogels for All-Solid-State Supercapacitors, ACS Appl. Mater. Interfaces. 13 (2021) 28222– 28230. https://doi.org/10.1021/acsami.1c05904.

[76] B. Talluri, M.L. Aparna, N. Sreenivasulu, S.S. Bhattacharya, T. Thomas, High entropy spinel metal oxide (CoCrFeMnNi)3O4 nanoparticles as a high-performance supercapacitor electrode material, J. Energy Storage. 42 (2021). https://doi.org/10.1016/j.est.2021.103004.